Phase Transitions ›
A Multinational Journal
Volume 96, 2023 - Issue 3-4

Full access

70 Views | 1 CrossRef citations to date | 0 Altmetric

Articles

SILAR-deposited manganese doped zinc oxide thin films for NO_2 gas detection applications

Nabeel T. Abood, Pradip B. Sable & Gopichand M. Dharne

Pages 274-289 | Received 05 Dec 2022, Accepted 07 Feb 2023, Published online: 28 Feb 2023

Cite this article https://doi.org/10.1080/01411594.2023.2179921 Check for updates

ABSTRACT

The structural, optical and gas detection characteristics of Mn-doped ZnO thin films synthesised by the Successive Ionic Layer Adsorption and Reaction (SILAR) process with varied doping concentrations (4, 6 and 8%) were examined. X-ray diffraction data was used to investigate the structural properties and confirm the hexagonal wurtzite crystal structure. The surface morphology and the existence of all elements were verified using a field emission scanning electron microscope and energy dispersive X-ray spectroscopy, respectively. To explore the vibrational bands present in Mn-doped ZnO films, we used FTIR spectra at ambient temperature. Ultraviolet-visible analysis reveals the absorption edge, which is found in the ultraviolet area, with a minor shift towards high wave length, whereas the energy bandgap

properties of Zn0.92Mn0.08O showed good sensitivity, selectivity and shorter response time when compared to other prepared films.

KEYWORDS: Metal oxide sensitivity selectivity gas sensor

1. Introduction

Nowadays, a slew of issues come to the attention of the public, one of which is the monitoring and detection of poisonous and hazardous gases such as CO, CO_2, CH_4, NO_2 and others in both industrial and home settings. Dangerous gases such as nitrogen dioxide (NO_2) are created during combustion in industries, thermal power plants, chemical facilities and motor vehicles [1]. It is extremely beneficial to build a NO_2 gas sensor with high sensitivity for detecting low NO_2 concentrations. Environmental monitoring and early warning systems can benefit from NO_2 gas sensors. Metal oxides, porous silicon and carbon nanotubes are utilised to make various materials and thin films for detecting NO_2 gas in ambient air [2].

Due to their superior optical, chemical and physical characteristics, metal oxide semiconductors have been widely used in the fabrication of gas sensors as a sensing material to detect harmful gases. The most commonly utilised materials for gas detection are metal oxides such as ZnO, SnO_2 and WO_3 [3–5].

ZnO is a prominent material of semiconductors used in a variety of applications such as gas sensing, optical, opto-electronic, piezoelectric, antibacterial activity, antifungal activity and photocatalytic devices [6–10]. Due to its relatively large surface area to volume ratio, wide band gap of 3.37 eV at room temperature, and high exciton binding energy, ZnO nanostructures have gained great attention in the field of gas sensing. Thus, it has become the best candidate among various metal oxide nanostructures [11].

Different techniques to improve the reaction speed and sensitivity of these metal oxide materials appear to have been devised. These include noble metal additions, metal oxide catalyst doping, the development of hybrid sensing materials, and the construction of nanostructures with enormous surface areas, various morphologies and nanoscale sizes [12].

In this article

working temperature of the ZnO sensor, as well as improving its selectivity, stability and fast response towards target gases. The morphology of the surface can be altered by doping, and the particle size of doped ZnO nanostructures is smaller than that of undoped ones due to host–dopant interaction, which prevents crystal growth [13]. Because doping with other elements is a proven method for regulating the amounts of donors and acceptors in semiconductors, it is frequently used to improve the gas sensing characteristics of metal oxide semiconductors [14].

The incorporation of a transition metal into a metal oxide semiconductor nanostructure improves electrical, magnetic and optical properties. Donor defects present in the material have an impact on the electrical and optical properties of transition metal doped metal oxide nanostructures. Additionally, it improves ferromagnetic and gas sensitive properties. As a result, the transition metal doped metal oxide semiconductor nanostructure is used in gas sensing [15].

Mn-doped ZnO exhibits high solid solubility without phase segregation due to the ionic radius of Mn^{2+} being extremely close to that of Zn^{2+} among transition metals, and Mn has exactly half-filled 3d orbitals that promote its assimilation into the ZnO lattice. In addition, Mn^{2+} doping creates additional states within the ZnO band gap [16,17]. By doping transition metals like Mn into ZnO nanostructures, ferromagnetic characteristics at room temperature may be obtained, which improves sensor device sensing capability [11]. ZnO's electrical, magnetic and optical characteristics benefit from Mn doping. As a result, ZnO doped with Mn has emerged as a viable option for diluted magnetic semiconductors. Applications for diluted magnetic semiconductor materials include their magneto-optical, magneto-electrical and magneto-transport capabilities, etc. [18].

Various prepared methods have been applied to the synthesis of Mn-doped ZnO films for different applications, such as the dip-coating sol-gel method [19], RF magnetron sputtering [20], spray pyrolysis [21], chemical bath deposition [16] and SILAR [22].

In comparison to other methods, the SILAR offers the best chance of producing a large-scale film at a reasonable cost for technological applications. It is appropriate for use at low temperatures and aids in the regulation of composition thickness and phase purity. Variations in deposition time and deposition cycles can also alter the characteristics of produced films

This article's goal is to study the structural, morphological, optical and sensing characteristics of thin films of Mn-doped ZnO fabricated using the SILAR method. According to our knowledge, we think this work represented a first attempt to use Mn-doped ZnO as a sensing material to detect NO_2 gas.

2. Experimental details

2.1. Synthesis of Mn-doped ZnO films

Zinc acetate dehydrate, ammonia solution and manganese acetate have been used as precursors for the preparation of Mn-doped ZnO thin films. For the deposition process, glass substrates have been used. Such substrates were first kept in a hot solution of chromic acid and then washed with detergent mixed with tap water and rinsed with acetone. Finally, it was washed with distilled water and dried at room temperature.

Zinc acetate and manganese acetate were dissolved in distilled water with the pH value adjusted to 11 by adding ammonia solution for the production of ($Zn_{1-x}Mn_xO$), where x = (0.04, 0.06 and 0.08) thin films. The precursor solution was swirled at room temperature for one hour until it became clear and homogenous. Pre-cleaned glass substrates were steeped in precursor solutions at 60°C for 30 s before being submerged in hot water at 60°C for another 30 s. The approach was done 30 times. The coated films are heated at 400°C in a muffle furnace for an hour at the end of the cycles to yield extremely crystalline Mn: ZnO thin films. Figure 1 shows the schematic diagram of the SILAR method.

Figure 1. Schematic diagram of SILAR method.

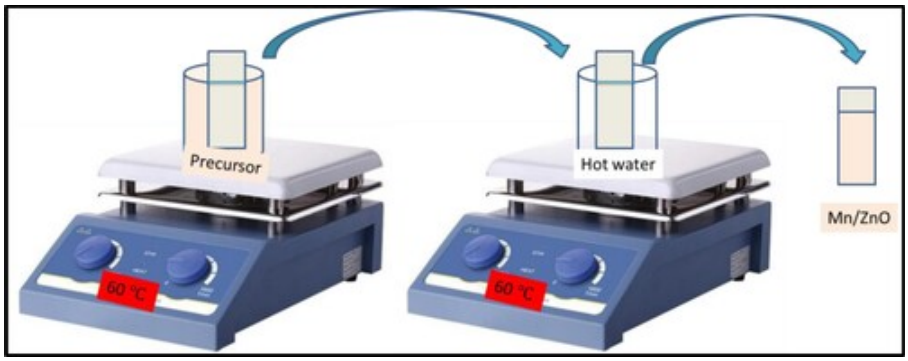

Display full size

In this article

To calculate the film thickness, the weight difference method was used as follows:

W_1 is the weight of the cleaned substrate. W_2 is the weight of the cleaned substrate plus film.
$W_2–W_1$ = the weight of the film
$\Delta W = mg$
$m = \Delta W / gm = \rho \times V$; where m is the mass of the film, ρ is the density of the film material and V is the volume of the film.
$\text{Volume} = (\text{Width} \times \text{Length} \times \text{Thickness})\text{of the film}.$

As a result, the thickness of the film = 'Volume'/('Width × Length)'.

The thicknesses of the three prepared films, $Zn_{0.96}Mn_{0.04}O$, $Zn_{0.94}Mn_{0.06}O$ and $Zn_{0.92}Mn_{0.08}O$ are found to be 1.8, 2.70 and 2.85 μm, respectively.

2.2. Gas sensing test

The gas sensing performance of Mn-doped ZnO films was investigated using a home-built static gas sensing device, which measured the change in resistance of the films in response to different NO_2 gas concentrations at a working temperature of 200°C. A sealed stainless steel test chamber with a capacity of 250 cm^3, a flat heating plate with a temperature controller, and a gas supply input (to enter gas) and output (to remove gas) are all part of the system. The film sensor's outside connections were wired into a Keithely 6514 electrometer with a computer-controlled data gathering system. A conducting silver paste was applied to both ends of a 1 cm × 2 cm film, which was then mounted on two probe sample holders and placed in a stainless steel test tube. Mn-doped ZnO thin films' resistance was measured in dry air flow prior to the addition of gas in order to establish the baseline resistance. Then, a microsyringe is used to inject a predetermined volume of gas into the housing. The following formula was used to determine the quantity of gas concentration that was injected:

$$\text{Conc. of test gas}\,(\text{ppm}) = \frac{volume\ of\ gas\ (ml) \times conc.\ of\ gas\ in\ chamber\ (1000\ ppm)}{volume\ of\ testing\ chamber\ (250\ ml)}$$

The gas response of sensor was calculated by using the relation:

$$S = \frac{R_g}{R_a} \quad (1)$$

Where R_a and R_g are resistances of the sensor in air and gas testing respectively.

In this article

3. Results and discussion

3.1. XRD analysis

The XRD patterns in the range 2θ (20^0–80^0) of $Zn_{1-x}Mn_xO$ (x = 0.04, 0.06 and 0.08) films are indicated in Figure 2. All films have a ZnO wurtzite structure that matches JCPDS card No. 36-1451 without any additional phases such as Mn or MnO, indicating that Mn doping has no effect on the ZnO wurtzite structure.

Figure 2. XRD patterns of (a) $Zn_{0.96}Mn_{0.04}O$ (b) $Zn_{0.94}Mn_{0.06}O$ (c) $Zn_{0.92}Mn_{0.08}O$.

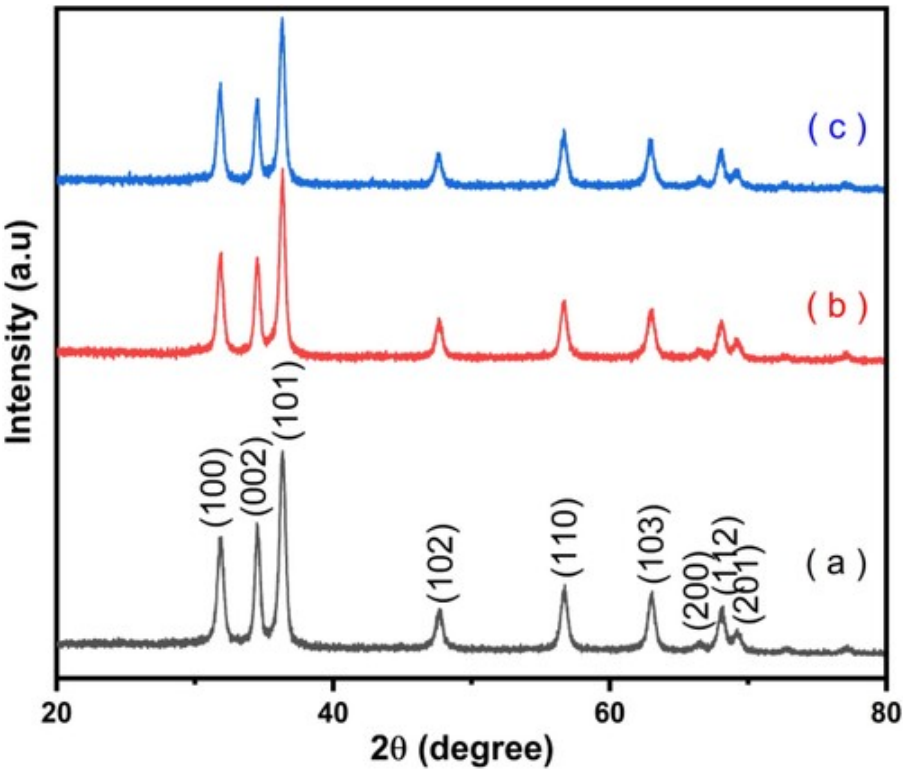

Display full size

The crystalline size of films was calculated by using Sherrer's equation:

$$D = \frac{0.9\lambda}{\beta COS\theta} \quad (2)$$

Where D is crystalline size, λ is wave length of incident X-ray, β is full width half maximum (FWHM) and θ is diffraction angle [25,26]. The crystalline size was found to increase with increasing of Mn doping concentration, which confirms the incorporation of Mn^{2+} (0.80 A^0) at the Zn^{2+} (0.74 A^0) sites [27–29]. A highly prominent (101) diffraction peak seen in XRD patterns

In this article

increasing dopant concentration, the breadth of the (100), (002) and (101) peaks decreases, leading in an increase in grain size. The narrowing of XRD peaks as a result of doping clearly suggests that Zn^{2+} has been effectively replaced by Mn^{2+} on the ZnO host thin film structure. Table 1, shows that the three main peaks positions, crystalline size and FWHM of prepared films.

Table 1. Peaks positions, FWHM and crystalline size of the three main peaks.

Download CSV Display Table

The lattice constants 'a' and ' c' can be estimated from the peaks (100) and (002) respectively by using the relations:

$$a = \frac{\lambda}{\sqrt{3}\sin\theta_{(100)}} \quad (3)$$

$$c = \frac{\lambda}{\sin\theta_{(002)}} \quad (4)$$

The unit cell volume can be calculated by using the equation.

$$V = 0.866 \times a^2 \times c \quad (5)$$

The obtained values of a and c as well as unit cell volume as shown in Table 2, show that as the Mn content increases, the lattice constants and unit volume increase. This is likely owing to the expansion of the lattice parameter caused by the substitution of the comparatively large ionic radii Mn^{2+} (0.80 A^0) ions at the smaller radii Zn^{2+} (0.74 A^0) sites, resulting in a modest rise in the lattice constants with the Mn contents [30].

Table 2. Lattice constants and unit cell volumes of prepared films.

Display Table

The density dislocation and micro strain can be determined from the relations:

$$\frac{1}{}$$

In this article

Where D is crystalline size.

$$\epsilon = \frac{\beta}{4\tan\theta} \quad (7)$$

Where β is full width at half maximum in radian and θ is diffraction angle in radian.

The calculated values showed decreased of density dislocation and microstrain with increase of Mn dopant concentrations as shows in Table 3.

Table 3. Average density dislocation and strain of films for three main peaks.

Download CSV Display Table

3.2. Morphological analysis

Figure 3(a–c) shows field emission scanning electron micrographs of Mn-doped ZnO. The presence of Mn at the Zn location has been discovered to affect the surface morphology of the films. The production of numerous spherical particles all over the surface of the Mn-doped ZnO film. The agglomeration of tiny grains into bigger clusters is seen, and this agglomeration is found to be increased with Mn doping as well as nanorod-like structures appearing in certain regions specifically in $Zn_{0.92}Mn_{0.08}O$ film, as illustrated in Figure 3(c). The movement of grain boundaries, which causes the coalescence of smaller grains for greater dopant concentrations, may be to blame for the rise in agglomeration.

Figure 3. FESEM micrographs of (a) $Zn_{0.96}Mn_{0.04}O$ (b) $Zn_{0.94}Mn_{0.06}O$ (c) $Zn_{0.92}Mn_{0.08}O$ and average particle size of (d) $Zn_{0.96}Mn_{0.04}O$ (e) $Zn_{0.94}Mn_{0.06}O$ (f) $Zn_{0.92}Mn_{0.08}O$.

In this article

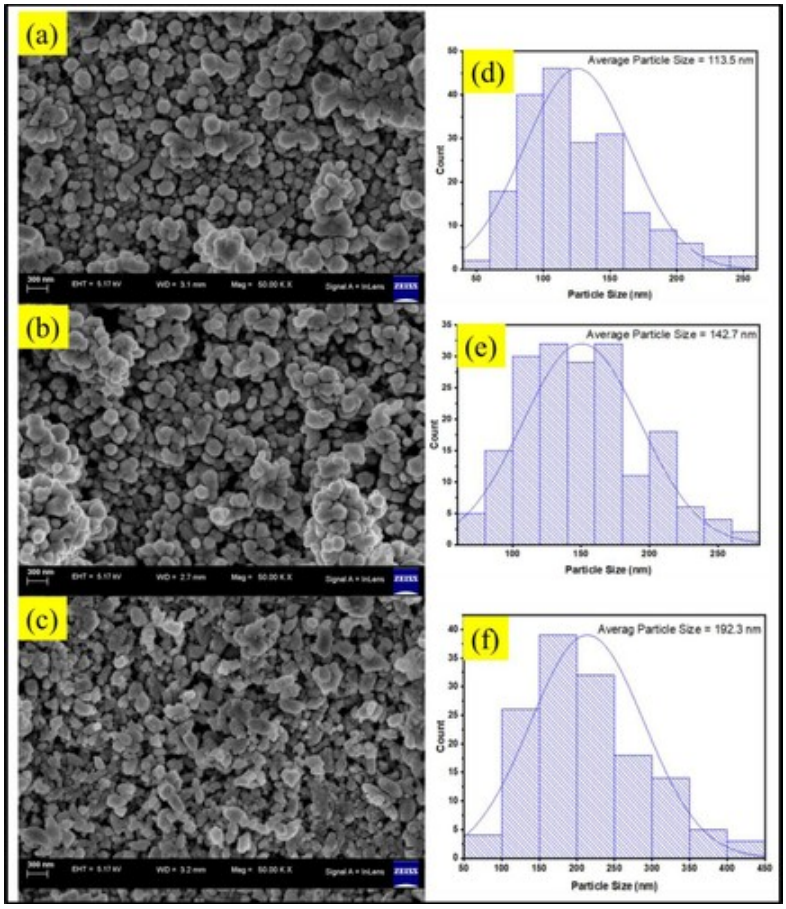

Display full size

Figure 3(d–f) shows the particle size of prepared sample $Zn_{0.96}Mn_{0.04}O$, $Zn_{0.94}Mn_{0.06}O$ and $Zn_{0.92}Mn_{0.08}O$, respectively.

3.3. EDS analysis

EDS was used to determine the manganese content of ZnO films produced on a glass substrate. The EDS analysis, as shown in Figure 4(a–c), demonstrated that the quantity of Mn incorporation is proportional to the amount of Mn concentration, as well as the dominance of oxygen in all samples with oxygen-rich stoichiometry.

Figure 4. EDS spectra of (a) $Zn_{0.96}Mn_{0.04}O$ (b) $Zn_{0.94}Mn_{0.06}O$ (c) $Zn_{0.92}Mn_{0.08}O$.

In this article

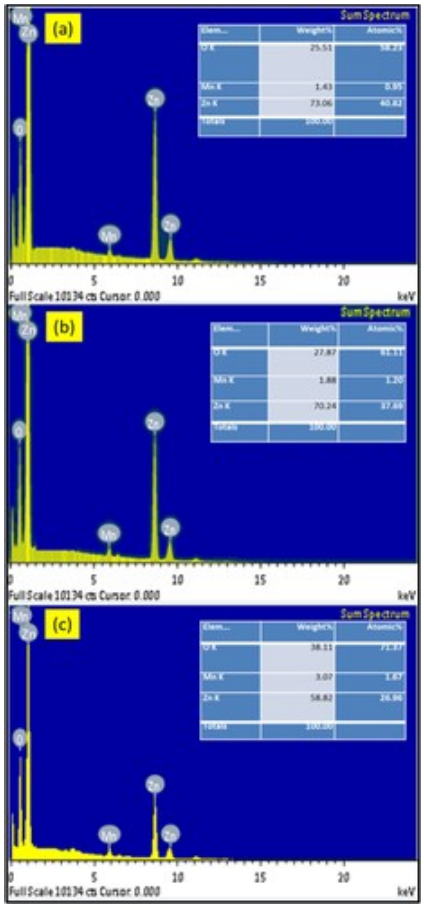

Display full size

3.4. FTIR analysis

FTIR spectra in the range 4000–600 cm^{-1} were used for the identification of functional groups and chemical bonds in the Mn-doped ZnO thin films. From the FTIR spectra as shown in Figure 5 (a–c), the peak at 3400 cm^{-1} is attributed to O–H stretching mode [31]. The peak located at 2896 cm^{-1} is due to asymmetric and symmetric vibration of C–H [27,31–33]. The peak around 2313 cm^{-1} is due to atmospheric CO_2 bound [34]. peaks at 1695 and 1518 cm^{-1} are attributed to asymmetric and symmetric C = O stretching, respectively [33]. The peak located at 1383 cm^{-1} may be attributed to the stretching vibration of CH_3 [35]. The band at 950 cm^{-1}–623 cm^{-1} of Mn-doped ZnO samples are due to the vibration of Zn-O and ZnMn-O [36].

Figure 5. FTIR spectra of (a) $Zn_{0.96}Mn_{0.04}O$ (b) $Zn_{0.94}Mn_{0.06}O$ (c) $Zn_{0.92}Mn_{0.08}O$.

In this article

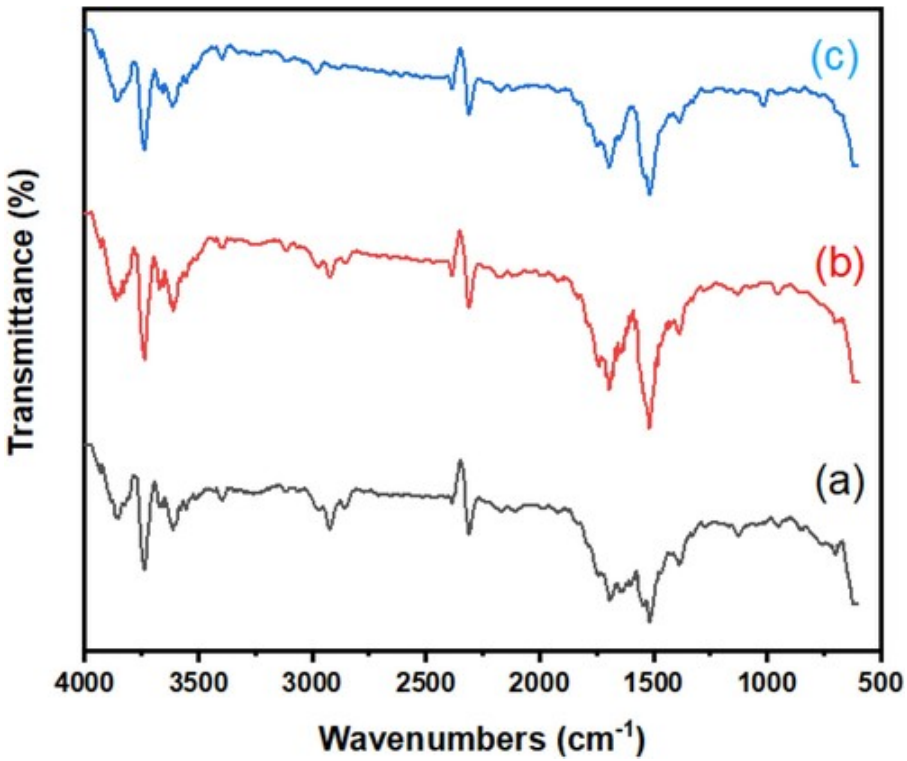

Display full size

3.5. UV-VIS analysis

As shown in Figure 6(a–c), the UV-Vis spectra of Mn doped ZnO thin films in the range 300–800 nm exhibit the absorption edge at 341, 360 and 361 nm, respectively. The absorption peaks show a shift towards high wavelengths with an increase of Mn dopant; this result agrees with that reported by [11,28].

Figure 6. UV-VIS spectra of (a) $Zn_{0.96}Mn_{0.04}O$ (b) $Zn_{0.94}Mn_{0.06}O$ (c) $Zn_{0.92}Mn_{0.08}O$.

In this article

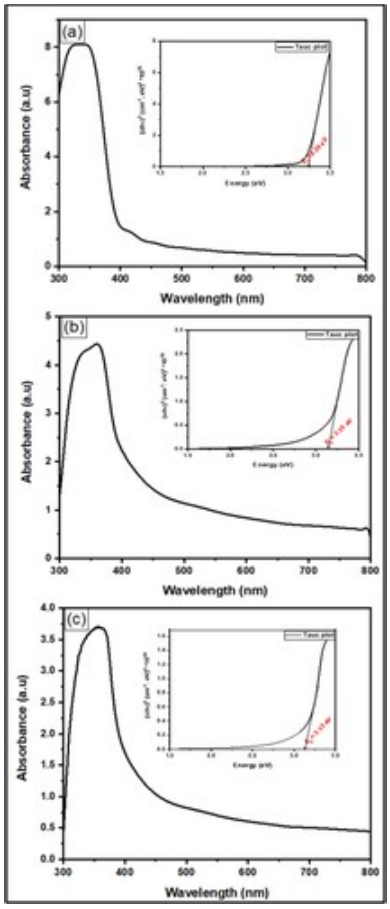

Display full size

The optical energy band gap was estimated by using Tauc's equation:
$\alpha h\nu = A(h\nu - E_g)^n$ (8) where α is the absorbance coefficient, hν is photon energy, E_g is the optical band gap, A is constant and n is the index, which can take the values 2 for indirect allowed, ½ for direct allowed, 3 for indirect forbidden and 1/3 for direct forbidden transition [37].

By plotting of $(\alpha h\nu)^2$ versus photon energy 'hν', as illustrated in the inserts in Figure 6(a–c). The linear segment of these plots, that intersect the energy axis at $(\alpha h\nu)^2 = 0$ yields the band gap energy 'Eg' [38]. Table 4 shows the values of the energy band gap. The results showed a decrease in energy band gap with increasing Mn concentration, It might be owing to the sp–d exchange interaction between transition metal ions and Zn or it could be due to Mn clustering, which results in a shift in average crystallite size and surface area-to-volume ratio [18,29,39].

Table 4. Energy band gap of prepared films.

In this article

Download CSV Display Table

3.6. Gas sensing properties

3.6.1. Sensitivity and response/recovery time

Rg/Ra and Ra/Rg are the gas responses to oxidising and reducing gases, respectively, where Ra is the sensor's resistance in air and Rg is the sensor's resistance in analytic gas. The first step in analysing a ‘metal oxide gas sensor’ is to establish the ideal operating temperature. Therefore, the Mn-doped ZnO samples are used to detect NO_2 gas at 40 ppm at different working temperatures in order to determine the ideal working temperature. The results are displayed in Figure 7. As can be observed from Figure 7, the sensitivity increases as the working temperature increases, peaking at 200°C. At temperatures above 200°C, the sensors’ responsiveness starts to decline. This indicates that the sensitivity of the Mn-doped ZnO thin film based sensor reduces as temperature increases. This may be because NO_2 gas molecules compete with oxygen atomic species for energetic locations on the metal oxide surface [40]. In the meantime, Figure 7 shows that for NO_2 gas detection with our ‘Mn-doped ZnO’ thin films, 200°C is the ideal working temperature.

Figure 7. Response of Mn-doped ZnO samples (a) $Zn_{0.96}Mn_{0.04}O$ (b) $Zn_{0.94}Mn_{0.06}O$ (c) $Zn_{0.92}Mn_{0.08}O$ towards 40 ppm concentration of NO_2 gas at different operating temperature.

In this article

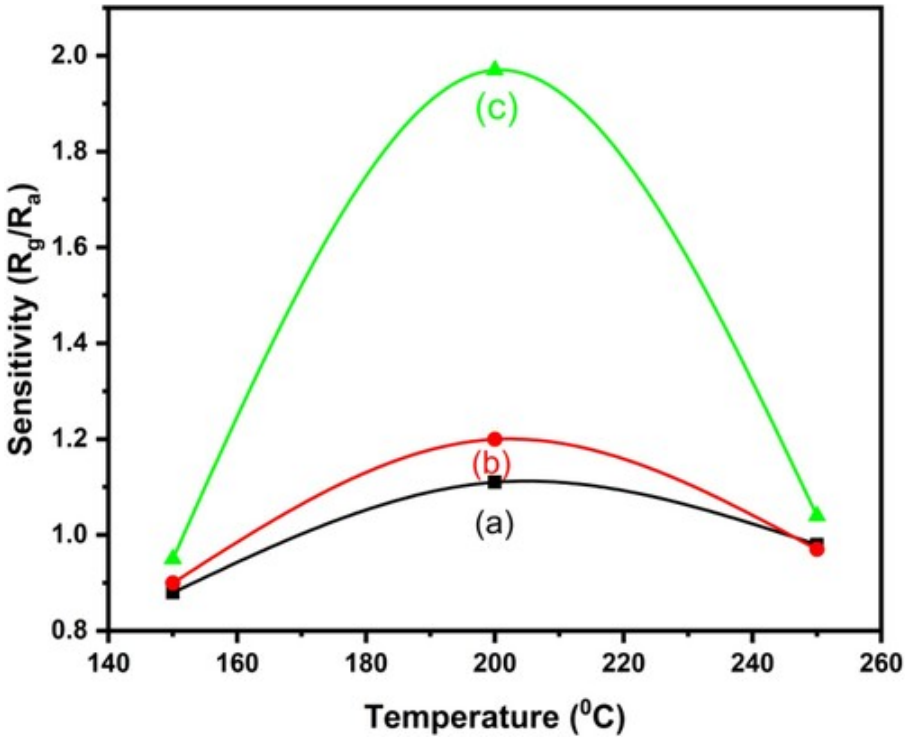

Display full size

Figure 8(a–c) shows the responses of prepared samples to a 40 ppm concentration of NO_2 gas at 200°C operating temperature, which were 1.11, 1.2 and 1.97 for the samples $Zn_{0.96}Mn_{0.04}O$, $Zn_{0.94}Mn_{0.06}O$ and $Zn_{0.92}Mn_{0.08}O$ respectively. The response of Mn/ZnO clearly increases with increasing Mn concentration. The highest response found to be 1.97 for the sample $Zn_{0.92}Mn_{0.08}O$. The nanorods which appear specifically in $Zn_{0.92}Mn_{0.08}O$ film as illustrated in Figure 3(c) may play an important role in performance of gas sensors is significantly influenced. Since there is only one electron transit route possible in the one-dimensional structure and longer nanorods have a bigger surface area, there is a free path for electron transport. As a result, nanorods have increased sensitivity. The calculated response/ recovery time of prepared films for 40 ppm NO_2 gas concentration were found to be 20.5/73.8 s, 15.22/192.5 s and 12.75/122 s for the prepared films $Zn_{0.96}Mn_{0.04}O$, $Zn_{0.94}Mn_{0.06}O$ and $Zn_{0.92}Mn_{0.08}O$ respectively. The response time was found to decrease as the Mn concentration increased. The film $Zn_{0.92}Mn_{0.08}O$ showed a shorter response time to 40 ppm NO_2 concentration around 12.75 s than others, which represented the film $Zn_{0.92}Mn_{0.08}O$ as an optimal candidate to use for detecting NO_2 gas. The calculated response and response/recovery time towards 40 ppm of NO_2 gas are listed in Table 5.

In this article

operating temperature (a) $Zn_{0.96}Mn_{0.04}O$ (b) $Zn_{0.94}Mn_{0.06}O$ (c) $Zn_{0.92}Mn_{0.08}O$.

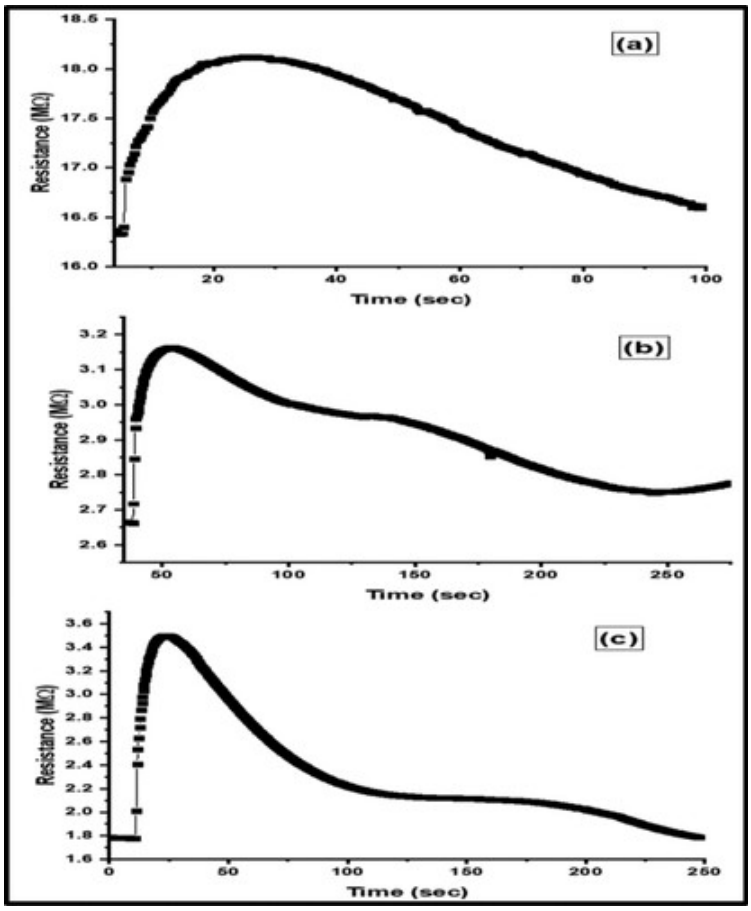

Display full size

Table 5. The response and response/recovery time of the prepared samples to wards 40 ppm of NO_2 gas at 200°C.

Display Table

For more characterisation, we used the film $Zn_{0.92}Mn_{0.08}O$ to study the response and response/recovery time at different NO_2 gas concentrations, as illustrated in Figure 9. From the figure, the response of film is found to be increased by increased of gas concentration, the values obtained by using the relation $S = \frac{R_g}{R_a}$ were found to be 1.97, 2.51, 2.73 and 2.92 at NO_2 gas concentrations 40, 60, 80 and 100 ppm respectively.

In this article

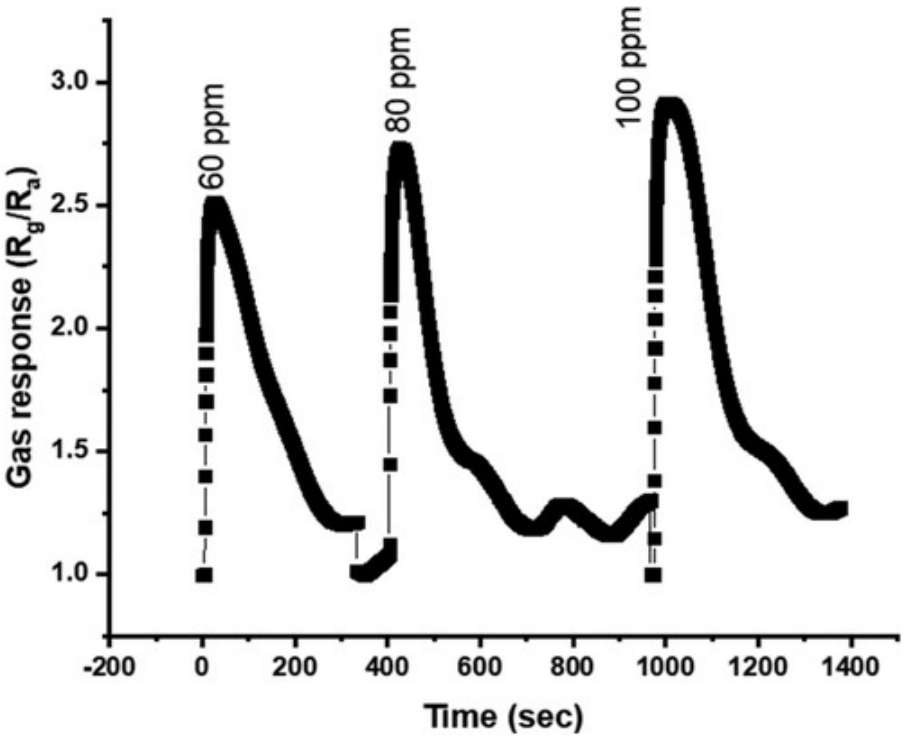

Display full size

The increase in response with increase of gas concentration is linear relationship can be attributed to increase of surface adsorption and reaction. The response/recovery time is found to be increased with increment of gas concentrations. Table 6, shows the response and response/recovery time of $Zn_{0.92}Mn_{0.08}O$, towards different concentrations of NO_2 gas at 200°C operating temperature as compared to various reported undoped and doped ZnO nanostructures.

Table 6. The response and response/recovery time of $Zn_{0.92}Mn_{0.08}O$ towards different concentration of NO_2 gas at 200°C, as compare to various reported undoped and doped ZnO nanostructures.

Display Table

3.6.2. Selectivity

The selectivity of gas sensors is one of the important parameters in gas sensing. The selectivity of prepared Zn0.92Mn0.08O was analysed at a 200°C operating temperature under 100 ppm of

In this article

of a Zn0.92Mn0.08O thin film towards various gases at a constant concentration of 100 ppm. The Zn0.92Mn0.08O shows a significant response to NO_2 gas compared to other gases, which were almost negligible compared to NO_2 gas. The sample showed greater selectivity toward NO_2 than other gases as a result of the oxygen-deficient sensor surface's increase in NO_2 adsorption sites. NO_2 species adsorb more quickly and effectively than other test gases due to their high reactivity and higher electron affinity (2.28 eV) in comparison to pre-adsorbed oxygen (0.43 eV) and other test gases [46].

Figure 10. Selectivity of $Zn_{0.92}Mn_{0.08}O$ thin film.

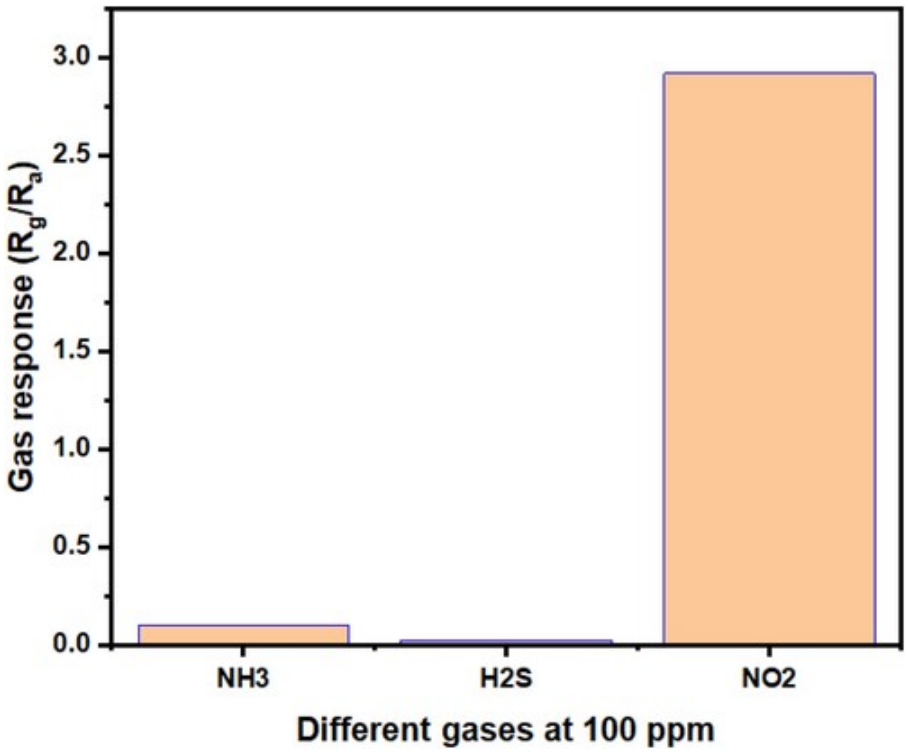

Display full size

3.6.3. Gas sensing mechanism

During the adsorption and desorption of target gas molecules on the sensing layer surface, the changes in electrical resistance of the sensing layer surface play an important role. As a result of this, the working principle of the Mn doped ZnO sensor in the presence of nitrogen dioxide gas is as follows: When oxygen molecules from the atmosphere are adsorbed on the surface of the sensing layer, they grab electrons from Mn/ZnO's conduction band, causing a drop in charge carrier concentration and a rise in the sensing layer's resistance [15]. This can happen in the

In this article

$O_{2gas} \rightarrow O_{2ads}$ (9)

$O_{2ads} + e^- \rightarrow O^-_{2ads}$ (10)

$O^-_{2ads} + e^- \rightarrow 2O^-_2$ (11)

$O^-_{ads} + e^- \rightarrow O^{-2}_{ads}$ (12)

Due to the oxidising nature of NO_2, NO_2 molecules either react with the oxygen species that are already adsorbed on the Mn/ZnO surface or trap electrons from the conduction band of Mn/ ZnO, which further increases resistance [1] as following reactions:

$NO_2 + e^- \rightarrow NO^-_2$ (13)

$NO_2 + O^-_2 + 2e^- \rightarrow NO^-_2 + 2O^-$ (14)

$NO_2 + O^- + 2e^- \rightarrow NO^-_2 + O^{-2}$ (15)

4. Conclusions

In this study, we successfully synthesised of Mn-doped ZnO thin films by using the SILAR method. The characterisation of the structural, morphological, elemental and optical characteristics of the Mn-doped ZnO was conducted using XRD, SEM, EDS, FTIR, and UV-Vis. All samples show hexagonal wurtzite crystal structures, according to XRD analysis. The size of the crystallite, the lattice constants, and the FWHM, point to Mn ions being substituted at the Zn site of the ZnO lattice. The FESEM images confirm numerous spherical particles all over the surface of the Mn doped ZnO film. The agglomeration of tiny grains into bigger clusters is seen, and this agglomeration is found to be increased with Mn doping. Zn, Mn, and oxygen are present across the scanned region of the samples, according to EDS spectra. FT-IR study confirms the proper incorporation of Mn ions in the Zn site of ZnO. UV–VIS analysis shows that the increase in Mn concentration causes a slight shift of the absorption edge and a decrease in the band gap. The response of Mn/ ZnO to 40 ppm of NO_2 gas increase with increment of Mn concentration. The highest response was found to be 1.97 for the sample $Zn_{0.92}$ $Mn_{0.08}$ O, with response/ recovery time 12.75/ 122 s. The response of Zn0.92 Mn0.08O to different NO_2 gas concentrations increases as the NO_2 gas concentration increases.

In this article

The authors extend their appreciation to the RUSA-Center for Advanced Sensor Technology, DR.BAM University Aurangabad, Punyashlok Ahilyadevi Holkar Solapur University/School of physical Sciences and Sprint Testing Solutions Mumbai, India, for characterisation techniques. The study's conception and design involved were contributed from all authors. Nabeel Thabet Abood handled the material preparation, data collecting, writing and analysis. Previous versions of the manuscript were discussed by the initial author and the other authors. The final manuscript was reviewed and approved by all authors.

Disclosure statement

No potential conflict of interest was reported by the author(s).

References

1. Kamble DL, Harale NS, Patil VL, et al. Characterization and NO2 gas sensing properties of spray pyrolyzed SnO2 thin films. J Anal Appl Pyrolysis. 2017;127:38–46.
Web of Science ® | Google Scholar

2. Burungale VV, Devan RS, Pawar SA, et al. Chemically synthesized PbS nanoparticulate thin films for a rapid NO2 gas sensor. Mater Sci-Poland. 2016;34:204–211.
Web of Science ® | Google Scholar

3. Kaur M, Shaheera M, Pathak A, et al. Highly sensitive NO2 sensor based on ZnO nanostructured thin film prepared by SILAR technique. Sens Actuators, B. 2021;335:129678.
Web of Science ® | Google Scholar

4. Xiao J, Che Y, Lv B, et al. Synthesis of WO 3 nanorods and their excellent ethanol Gas-sensing performance. Mater Res. 2021: 24.
Web of Science ® | Google Scholar

5. Gattu KP, Kashale AA, Ghule K, et al. NO2 sensing studies of bio-green synthesized Au-doped SnO2. J Mater Sci: Mater Electron. 2017;28:13209–13216.
Web of Science ® | Google Scholar

6. Mahajan SV, Upadhye DS, Shaikh SU, et al. Mn doped nanostructure ZnO thin film for photo sensor and gas sensor application. 2013.
Google Scholar

7. Fatima AA, Devadason S, Mahalingam T. Structural, luminescence and magnetic properties of Mn doped ZnO thin films using spin coating technique. J Mater Sci: Mater Electron. 2014;25:3466–3472.
Web of Science ® | Google Scholar

8. Haque M, Fouad H, Seo H-K, et al. Investigation of Mn doped ZnO nanoparticles towards ascertaining myocardial infarction through an electrochemical detection of myoglobin. IEEE Access. 2020;8:164678–164692.
Web of Science ® | Google Scholar

9. Mozammel M, Ilkhechi NN, Ghezelbash B, et al. Antibacterial and heavy ion removal properties of La-and Ti-doped ZnO nanoparticles. Mater Res Express. 2019;6:085010.
Web of Science ® | Google Scholar

10. Ilkhechi NN, Mozammel M, Khosroushahi AY. Antifungal effects of ZnO, TiO2 and ZnO-TiO2 nanostructures on Aspergillus flavus. Pestic Biochem Physiol. 2021;176:104869.
PubMed | Web of Science ® | Google Scholar

11. Ganesh RS, Durgadevi E, Navaneethan M, et al. Low temperature ammonia gas sensor based on Mn-doped ZnO nanoparticle decorated microspheres. J Alloys Compd. 2017;721:182–190.
Web of Science ® | Google Scholar

12. Gawali SR, Patil VL, Deonikar VG, et al. Ce doped NiO nanoparticles as selective NO2 gas sensor. J Phys Chem Solids. 2018;114:28–35.

Web of Science ® | Google Scholar

13. Bhati VS, Hojamberdiev M, Kumar M. Enhanced sensing performance of ZnO nanostructures-based gas sensors: A review. Energy Reports. 2020;6:46–62.
Web of Science ® | Google Scholar

14. Ahmed F, Arshi N, Anwar M, et al. Mn-doped ZnO nanorod gas sensor for oxygen detection. Curr Appl Phys. 2013;13:S64–SS8.
Web of Science ® | Google Scholar

15. Ganesh RS, Durgadevi E, Navaneethan M, et al. Controlled synthesis of Ni-doped ZnO hexagonal microdiscs and their gas sensing properties at low temperature. Chem Phys Lett. 2017;689:92–99.
Web of Science ® | Google Scholar

16. Fang J, Luo W, Hsu C, et al. The transparent conductive properties of manganese-doped zinc oxide films deposited by chemical bath deposition. J Electron Mater. 2012;41:122–129.
Web of Science ® | Google Scholar

17. Pham HN, Tong MH, Huynh HQ, et al. The enhancement of visible photodetector performance based on Mn doped ZnO nanorods by substrate architecting. Sens Actuators, A. 2020;311:112085.
Web of Science ® | Google Scholar

18. Mote V, Dargad J, Dole B. Effect of Mn doping concentration on structural, morphological and optical studies of ZnO nano-particles. Nanosci Nanoeng. 2013;1:116–122.
Google Scholar

19. Merzouk H, Chelouche A, Saoudi S, et al. Influence of Mn doping on structural and optical properties of ZnO nano thin films synthesized by sol–gel technique. Appl Phys A. 2012;109:841–844.

20. Elanchezhiyan J, Bhuvana K, Gopalakrishnan N, et al. Investigation on Mn doped ZnO thin films grown by RF magnetron sputtering. Mater Lett. 2008;62:3379–3381.
Web of Science ® | Google Scholar

21. Singh B, Shrivastava S, Ganesan V. Effects of Mn doping on zinc oxide films prepared by spray pyrolysis technique. Int J Nanosci. 2017;16:1650024.
Google Scholar

22. Mondal S, Bhattacharyya S, Mitra P. Preparation of manganese-doped ZnO thin films and their characterization. Bull Mater Sci. 2013;36:223–229.
Web of Science ® | Google Scholar

23. Devi KR, Selvan G, Karunakaran M, et al. SILAR-coated Mg-doped ZnO thin films for ammonia vapor sensing applications. J Mater Sci: Mater Electron. 2020;31:10186–10195.
Web of Science ® | Google Scholar

24. Patil A, Patil R, Lohar G, et al. Facile synthesis of CuO nanostructures for non-enzymatic glucose sensor by modified SILAR method. Appl Phys A. 2021;127:1–10.
Web of Science ® | Google Scholar

25. Ilkhechi NN, Kaleji BK. Temperature stability and photocatalytic activity of nanocrystalline cristobalite powders with Cu dopant. Silicon. 2017;9:943–948.
Web of Science ® | Google Scholar

26. Ilkhechi NN, Ghobadi N. Comparison of structural, optical, photocatalytic behavior and hydrophilic properties of pure and Sn/La co-doped TiO2 thin films. J Mater Sci: Mater Electron. 2016;27:12050–12059.
Web of Science ® | Google Scholar

27. Raskar ND, Dake DV, Mane VA, et al. One step synthesis of vertically grown Mn-doped ZnO nanorods for photocatalytic application. J Mater Sci: Mater Electron. 2019;30:10886–10899.

In this article

28. Sharma M, Bera K, Mishra R, et al. Structural, magnetic, and optical properties of Mn2+ doping in ZnO thin films. Surfaces. 2021;4:268–278.
Google Scholar

29. Kumar P, Singh BK, Pal BN, et al. Correlation between structural, optical and magnetic properties of Mn-doped ZnO. Appl Phys A. 2016;122:1–12.
Web of Science ® | Google Scholar

30. Hu D, Liu X, Deng S, et al. Structural and optical properties of Mn-doped ZnO nanocrystalline thin films with the different dopant concentrations. Physica E. 2014;61:14–22.
Google Scholar

31. Gu P, Zhu X, Yang D. Structural, optical and photoelectric properties of Mn-doped ZnO films used for ultraviolet detectors. RSC Adv. 2019;9:8039–8047.
PubMed | Web of Science ® | Google Scholar

32. Singh AK, Thool GS, Bangal PR, et al. Low temperature Mn doped ZnO nanorod array: synthesis and its photoluminescence behavior. Ind Eng Chem Res. 2014;53:9383–9390.
Web of Science ® | Google Scholar

33. Tan TL, Lai CW, Hamid A, et al. Tunable band gap energy of Mn-doped ZnO nanoparticles using the coprecipitation technique. J Nanomater. 2014;2014.
Web of Science ® | Google Scholar

34. Senthilkumaar S, Rajendran K, Banerjee S, et al. Influence of Mn doping on the microstructure and optical property of ZnO. Mater Sci Semicond Process. 2008;11:6–12.
Web of Science ® | Google Scholar

35. Hao Y-M, Lou S-Y, Zhou S-M, et al. Structural, optical, and magnetic studies of manganese-doped zinc oxide hierarchical microspheres by self-assembly of nanoparticles. Nanoscale Res Lett. 2012;7:1–9.

36. Mote V, Purushotham Y, Dole B. Structural, morphological, physical and dielectric properties of Mn doped ZnO nanocrystals synthesized by sol–gel method. Mater Des. 2016;96:99–105.
Web of Science ® | Google Scholar

37. Mir FA. Transparent wide band gap crystals follow indirect allowed transition and bipolaron hopping mechanism. Results Phys. 2014;4:103–104.
Web of Science ® | Google Scholar

38. Ilkhechi NN, Aghjehkohal AR, TanourAghaj EF, et al. Enhanced optical and hydrophilic properties of Si and Cd co-doped TiO2 thin films. J Mater Sci: Mater Electron. 2017;28:4598–4605.
Web of Science ® | Google Scholar

39. Omri K, El Ghoul J, Lemine O, et al. Magnetic and optical properties of manganese doped ZnO nanoparticles synthesized by sol–gel technique. Superlattices Microstruct. 2013;60:139–147.
Web of Science ® | Google Scholar

40. Patil V, Vanalakar S, Tarwal N, et al. Construction of Cu doped ZnO nanorods by chemical method for Low temperature detection of NO2 gas. Sens Actuators, A. 2019;299:111611.
Web of Science ® | Google Scholar

41. Chougule M, Sen S, Patil V. Fabrication of nanostructured ZnO thin film sensor for NO2 monitoring. Ceram Int. 2012;38:2685–2692.
Web of Science ® | Google Scholar

42. Chebil W, Boukadhaba M, Madhi I, et al. Structural, optical and NO2 gas sensing properties of ZnMgO thin films prepared by the sol gel method. Phys B. 2017;505:9–16.
Web of Science ® | Google Scholar

43. Kamble V, Navale Y, Patil V, et al. Enhanced NO 2 gas sensing performance of Ni-doped ZnO nanostructures. J Mater Sci: Mater Electron. 2021;32:2219–2233.

44. Chougule M, Nalage S, Sen S, et al. Development of nanostructured ZnO thin film sensor for NO2 detection. J Exp Nanosci. 2014;9:482–490.

Web of Science ® | Google Scholar

45. Abood N, Sable P, Yassen J, et al. Fabrication of ZnO nanorods structure for drastically enhancing gas sensing response to NO2 Gas. Trends Sci. 2022;19:1965.

Google Scholar

46. Patil M, Ganbavle V, Rajpure K, et al. Fast response and highly selective nitrogen dioxide gas sensor based on zinc stannate thin films. Mater Sci Energy Technol. 2020;3:36–42.

Google Scholar